Journal of Computational Physics 458 (2022) 111097

Contents lists available at ScienceDirect

Journal of Computational Physics

www.elsevier.com/locate/jcp

A new class of higher-order decoupled schemes for the incompressible Navier-Stokes equations and applications to rotating dynamics

Ke Wu [a], Fukeng Huang [b], Jie Shen [a,*,1]

[a] Department of Mathematics, Purdue University, West Lafayette, IN 47906, USA
[b] Department of Mathematics, National University of Singapore, 119076, Singapore

ARTICLE INFO

Article history:
Received 3 September 2021
Received in revised form 7 February 2022
Accepted 20 February 2022
Available online 25 February 2022

Keywords:
Navier-Stokes
Rotating flow
SAV
Stability
Legendre-Galerkin

ABSTRACT

A new class of time discretization schemes for the Navier-Stokes equations with non-periodic boundary conditions is constructed by combining the SAV approach for general dissipative systems in [15] and the consistent splitting schemes in [10]. The new schemes are unconditionally stable, only require solving linear equations with constant coefficients at each time step, and can be up to six-order accurate in time. With a Legendre-Galerkin method in space, the full discretized schemes can efficiently treat the Coriolis force implicitly. Delicate numerical simulations for highly complex rotating flows are presented to validate the new schemes.

1. Introduction

Numerical approximation of the incompressible Navier-Stokes equations plays an important role in computational fluid dynamics, and has been a subject of intensive study since the sixties. There is an ever increasing demand for numerical algorithms which can efficiently and accurately capture the complex dynamics or turbulence statistics of incompressible flows. A large body of the literature has been devoted to construct various numerical algorithms for solving the incompressible Navier-Stokes equations, see [29,4,5,13,23] and the references therein. In particular, the projection method or fractional step method, originally proposed by Chorin [3] and Temam [28], and its various variants and improvements have been widely used thanks to its simplicity and efficiency, see [9] and references therein. Almost exclusively these schemes are restricted to first- or second-order accuracy in time, due in part to their operator-splitting nature with non-commutative operators, see however [17] for a third-order operator splitting scheme, which is later classified the velocity-correction method in [11], and [12] for high-order splitting schemes based on the artificial compressibility method which requires solving a non-separable system involving the $\nabla\nabla\cdot$ operator.

Recently, the scalar auxiliary variable (SAV) approach for constructing efficient and stable time discretization schemes for gradient flows is proposed in [25,26], and is extended to Navier-Stokes equations in [20,19]. The original SAV approach allows us to construct linear, decoupled and unconditionally stable and up to second-order schemes. In [15], the authors

* Corresponding author.
E-mail addresses: wu1589@purdue.edu (K. Wu), hfkeng@nus.edu.sg (F. Huang), shen7@purdue.edu (J. Shen).

[1] The work of this author is supported in part by AFOSR grant FA9550-20-1-0309 and NSF grant DMS-2012585.

https://doi.org/10.1016/j.jcp.2022.111097
0021-9991/

introduced a SAV approach to construct higher-order unconditionally stable schemes for general dissipative systems. This approach is successfully applied to Navier-Stokes equations with periodic boundary conditions in [14]. From a numerical point of view, it is much easier to design numerical algorithms for the Navier-Stokes equations with periodic boundary conditions due to the fact that the pressure can be explicitly expressed as a function of the velocity as no additional boundary condition is needed for the pressure. A main difficulty for the numerical approximation of the Navier-Stokes equations with non-periodic boundary conditions is the lack of explicit boundary condition for the pressure. Most projection type schemes, in one way or another, attempt to find a good approximation to the pressure boundary conditions [9]. In [10] (see also [22]), a consistent splitting approach was proposed. This approach is based on a consistent pressure Poisson equation, and is free of large splitting error due to the approximate pressure boundary conditions associated with other projection type methods, higher-order consistent splitting schemes can be formally constructed. But unfortunately, one can only prove a rigorous stability result for the first-order scheme (see [10] and [22]). The first objective of this paper is to combine the approach in [15] for general dissipative systems and the consistent splitting approach in [10] to construct a class of efficient schemes, with up to six-order accuracy in time, for the Navier-Stokes equations with non-periodic boundary conditions, and to prove its stability.

The second objective of this paper is to validate this new class of numerical schemes by simulating a real world geophysical flow problem with complex spatial-temporal structures that requires highly accurate and efficient numerical algorithms. Particularly, we are interested in parametrically forced rotating confined flows, which model the rotational dynamics of planets and stars involve periodic perturbations of shapes, the directions of rotational vectors, and rotation rates. These perturbations are categorized as tides, precession, and longitudinal libration in terms of geophysical flows, as articulated in the review paper [18]. Using a sequence of well designed flow simulations, we will show that the proposed SAV schemes implemented with Legendre-Galerkin method in space outperform the reference scheme, an improved second-order projection scheme with a spectral-collocation method in space, in terms of accuracy and efficiency. And our extensive simulations suggest that the third-order SAV scheme with Legendre-Galerkin method in space is the most efficient while highly complex spatial-temporal structures are present.

One salient feature of the geophysical flows is that the associated Ekman number, $E = \nu/(\Omega_0 L^2)$, is extremely small (corresponding to very large Reynolds number), where ν is the viscosity of the fluid, Ω_0 is the background rotation rate and L is the length scale of the computational domain. For instance, the Ekman number of Earth's inner core is on the order of 10^{-15}, which presents a great challenge for its numerical simulation. Parameters used in the state-of-the-art simulations [33,21,32] are far away from the realistic parameters due to the high computational cost and limited accuracy of the numerical schemes. In addition, these flows are driven by external mechanical forcing, which converts part of the background rotational energy and generates intense fluid motions through the excitation of localized jets, shear layers and resonant inertial modes [18]. In this scenario, the numerical scheme not only needs to resolve very thin boundary layers, but also to capture the intense shear layers and the inertial modes in the interior of the computational domain. Currently, majority of the simulations are conducted at the Ekman number $E \leq 10^{-6}$, and very few are conducted at $E = 10^{-7}$, such as libration-driven flows in spherical shells [21] and in a cube [32]. The Coriolis force in these simulations is all treated explicitly which dictates a very several time step constraints due to the high background rotation. The third objective is to implement a Legendre-Galerkin method which can treat the Coriolis force implicitly with essentially the same computational cost, and use the validated third-order SAV scheme with this Legendre-Galerkin method to simulate the rotating flows with the Ekman number at least one order of magnitude lower, e.g. $E \leq 10^{-8}$.

The rest of the paper is organized as follows. In the next section, we describe the Navier-Stokes equations in inertial frame and in rotational frame, present our time and spatial discretization, provide a stability proof and carry out accuracy tests for a manufactured solution. In Section 3, we validate the new schemes with detailed simulations of rotating flows in three different settings: a librating cube with rotation axis $(0, 0, 1)$, a librating cube with rotation axis $(1, 1, 1)/\sqrt{3}$, and a precessing cube with a precessing angle $\alpha = 1$ degree. Some concluding remarks are given in the last section.

2. Problem description and the numerical schemes

We consider numerical approximation of the Navier-Stokes equations in the inertial reference frame:

$$\frac{\partial \boldsymbol{u}}{\partial t} + \boldsymbol{u}\cdot\nabla\boldsymbol{u} - \nu\Delta\boldsymbol{u} = -\nabla p + \boldsymbol{f}, \tag{1a}$$

$$\nabla\cdot\boldsymbol{u} = 0, \tag{1b}$$

in an open bounded domain $D \subset R^d (d = 2, 3)$, where $\boldsymbol{f}$ is an external force, and in the rotating reference frame:

$$\frac{\partial \boldsymbol{u}}{\partial t} + \boldsymbol{u}\cdot\nabla\boldsymbol{u} + 2\boldsymbol{\Omega}\times\boldsymbol{u} - \nu\Delta\boldsymbol{u} = -\nabla p + \boldsymbol{f}, \tag{2a}$$

$$\nabla\cdot\boldsymbol{u} = 0, \tag{2b}$$

where Ω is a given background rotating velocity, $\boldsymbol{\Omega}\times\boldsymbol{u}$ represents the Coriolis force, and $\boldsymbol{f} = \frac{d\boldsymbol{\Omega}}{dt}\times\boldsymbol{r}$ represents the Euler force with $\boldsymbol{r} = (x, y, z)$. Both systems are subjected to suitable boundary and initial conditions for the velocity. To simplify

the presentation, we only consider the no slip boundary conditions for the velocity, although other boundary conditions can be treated similarly. Setting $\Omega = 0$ in (2), we recover (1). Hence, we shall only consider the system (2) and treat (1) as a special case of (2).

Let $\boldsymbol{n}$ be the outward normal to D, and denote

$$\boldsymbol{H} = \{\boldsymbol{v} \in (L^2(D))^d : \nabla \cdot \boldsymbol{v} = 0,\ \boldsymbol{v} \cdot \boldsymbol{n}|_{\partial D} = 0\}. \tag{3}$$

Thanks to the identity

$$(\boldsymbol{u} \cdot \nabla \boldsymbol{v}, \boldsymbol{v}) = 0 \quad \forall \boldsymbol{u} \in \boldsymbol{H},\ \boldsymbol{v} \in (H_0^1(D))^d, \tag{4}$$

it is easy to see that (2) with no slip boundary conditions satisfies the following energy law:

$$\frac{d}{dt}\frac{1}{2}\|\boldsymbol{u}\|^2 = -\nu\|\nabla \boldsymbol{u}\|^2 + (\boldsymbol{f}, \boldsymbol{u}). \tag{5}$$

2.1. Time discretization by a SAV approach

Set $E(\boldsymbol{u}) = \frac{1}{2}\|\boldsymbol{u}\|^2$ and define a SAV: $R(t) = E(\boldsymbol{u}) + C_0$ with some $C_0 > 0$, and expand the Navier-Stokes equations (2) as

$$\frac{\partial \boldsymbol{u}}{\partial t} + \boldsymbol{u} \cdot \nabla \boldsymbol{u} + 2\boldsymbol{\Omega} \times \boldsymbol{u} - \nu \Delta \boldsymbol{u} = -\nabla p + \boldsymbol{f}, \tag{6a}$$

$$\nabla \cdot \boldsymbol{u} = 0, \tag{6b}$$

$$\frac{\partial R}{\partial t} = \frac{R}{E(\boldsymbol{u}) + C_0}[-\nu\|\nabla \boldsymbol{u}\|^2 + (\boldsymbol{f}, \boldsymbol{u})]. \tag{6c}$$

It is clear that any solution of the original Navier-Stokes equations (1) is a solution of the above system with $R(0) = -\nu\|\nabla \boldsymbol{u}|_{t=0}\|^2 + (\boldsymbol{f}, \boldsymbol{u})|_{t=0}$. Inspired by the SAV approach proposed in [25,26] and the consistent splitting scheme in [10], we construct the following k-th ($1 \le k \le 6$) order SAV schemes based on the BDF-k for the time derivative.

Given R^j, $\boldsymbol{u}^j$ ($j = n, n-1, \cdots, n-k+1$), we compute $\bar{\boldsymbol{u}}^{n+1}$, R^{n+1}, ξ^{n+1}, $\boldsymbol{u}^{n+1}$ and p^{n+1} consecutively as follows

$$\frac{\alpha_k \bar{\boldsymbol{u}}^{n+1} - A_k(\bar{\boldsymbol{u}}^n)}{\delta t} - \nu \Delta \bar{\boldsymbol{u}}^{n+1} + 2\Omega^{n+1} \times \hat{\boldsymbol{u}}^{n+1} = -B_k(\boldsymbol{u}^n) \cdot \nabla B_k(\boldsymbol{u}^n) + \nabla B_k(p^n) + \boldsymbol{f}^{n+1}; \tag{7a}$$

$$\frac{1}{\delta t}\left(R^{n+1} - R^n\right) = \frac{R^{n+1}}{E(\bar{\boldsymbol{u}}^{n+1}) + C_0}(-\nu\|\nabla \bar{\boldsymbol{u}}^{n+1}\|^2 + (\boldsymbol{f}^{n+1}, \bar{\boldsymbol{u}}^{n+1})); \tag{7b}$$

$$\boldsymbol{u}^{n+1} = \eta_k^{n+1}\bar{\boldsymbol{u}}^{n+1} \ \text{ with } \eta_k^{n+1} = 1 - (1 - \xi^{n+1})^k \ \text{ and } \ \xi^{n+1} = \frac{R^{n+1}}{E(\bar{\boldsymbol{u}}^{n+1}) + C_0}; \tag{7c}$$

$$\langle \nabla p^{n+1}, \nabla q\rangle = \langle \boldsymbol{f}^{n+1} - \boldsymbol{u}^{n+1} \cdot \nabla \boldsymbol{u}^{n+1} - 2\Omega^{n+1} \times \boldsymbol{u}^{n+1} - \nu \nabla \times \nabla \times \boldsymbol{u}^{n+1}, \nabla q\rangle, \tag{7d}$$

where we can set $\hat{\boldsymbol{u}}^{n+1} = \bar{\boldsymbol{u}}^{n+1}$, i.e., the Coriolis force is treated implicitly; or $\hat{\boldsymbol{u}}^{n+1} = B_k(\boldsymbol{u}^n)$, i.e., the Coriolis force is treated explicitly.

In the above, α_k, the operators A_k and B_k ($k = 1, 2, 3$), with a slight abuse of notations, are given by:

first-order:

$$\alpha_1 = 1, \quad A_1(\boldsymbol{u}^n) = \boldsymbol{u}^n, \quad B_1(\bar{\boldsymbol{u}}^n) = \bar{u}^n; \tag{8}$$

second-order:

$$\alpha_2 = \frac{3}{2}, \quad A_2(\boldsymbol{u}^n) = 2\boldsymbol{u}^n - \frac{1}{2}\boldsymbol{u}^{n-1}, \quad B_2(\bar{\boldsymbol{u}}^n) = 2\bar{\boldsymbol{u}}^n - \bar{\boldsymbol{u}}^{n-1}; \tag{9}$$

third-order:

$$\alpha_3 = \frac{11}{6}, \quad A_3(\boldsymbol{u}^n) = 3\boldsymbol{u}^n - \frac{3}{2}\boldsymbol{u}^{n-1} + \frac{1}{3}\boldsymbol{u}^{n-2}, \quad B_3(\bar{\boldsymbol{u}}^n) = 3\bar{\boldsymbol{u}}^n - 3\bar{\boldsymbol{u}}^{n-1} + \bar{\boldsymbol{u}}^{n-2}. \tag{10}$$

The formulae for $k = 4, 5, 6$ can also be readily derived. Several remarks are in order:

- $\bar{\boldsymbol{u}}^{n+1}$ is determined by a usual k-th order semi-implicit scheme (7a).
- We observe that R^{n+1} is a first-order approximation to $E(u(\cdot, t_{n+1})) + C_0$ which implies that ξ^{n+1} is a first-order approximation to 1. Hence, η_k^{n+1} is a k-th order approximation to 1, and $\boldsymbol{u}^{n+1}$ is a k-th order correction to $\bar{\boldsymbol{u}}^{n+1}$.
- The main computational cost is to solve the linear system (7a) and a pressure Poisson equation (7d). With $\hat{\boldsymbol{u}}^{n+1} = B_k(\boldsymbol{u}^n)$, (7a) reduces to decoupled Poisson type equations for each component of $\bar{\boldsymbol{u}}^{n+1}$, while with $\hat{\boldsymbol{u}}^{n+1} = \bar{\boldsymbol{u}}^{n+1}$, the components of $\bar{\boldsymbol{u}}^{n+1}$ are coupled in (7a), making it more difficult to solve.

- In practice, the term $\langle \nabla \times \nabla \times \boldsymbol{u}^{n+1}, \nabla q \rangle$ can be computed as follows:
  Let $\boldsymbol{\omega} = \nabla \times \boldsymbol{u}$ be the vorticity field of the flow, then $\nabla \times \nabla \times \boldsymbol{u} = \nabla \times \omega$.

$$\langle \nabla \times \nabla \times \boldsymbol{u}, \nabla q \rangle = \langle \nabla \times \omega, \nabla q \rangle = \int_{\partial D} (\omega \times \nabla q) \cdot \boldsymbol{n} ds, \tag{11}$$

  where $\boldsymbol{n}$ is the outward normal of ∂D.

2.2. Spatial discretization

We first consider a generic spatial discretization as follows. Let $X_h \subset H_0^1(D)$, $\boldsymbol{X}_h = (X_h)^d$ and $Q_h \subset H^1(D)$ be a pair of finite dimensional spaces. The fully discrete version of the scheme (7) is: Find $\boldsymbol{u}_h^{n+1} \in \boldsymbol{X}_h$ and $p_h^{n+1} \in Q_h$ from:

$$\begin{aligned}
&(\frac{\alpha_k \bar{\boldsymbol{u}}_h^{n+1} - A_k(\bar{\boldsymbol{u}}_h^n)}{\delta t}, \boldsymbol{v}_h) + \nu(\nabla \bar{\boldsymbol{u}}_h^{n+1}, \nabla \boldsymbol{v}_h) \\
&\qquad + 2(\Omega^{n+1} \times \hat{\boldsymbol{u}}_h^{n+1}, \boldsymbol{v}_h) = (-B_k(\boldsymbol{u}_h^n) \cdot \nabla B_k(\boldsymbol{u}_h^n) + \nabla B_k(p_h^n) + \boldsymbol{f}^{n+1}, \boldsymbol{v}_h), \ \forall \boldsymbol{v}_h \in \boldsymbol{X}_h, \qquad (12a)\\
&\frac{1}{\delta t}\big(R^{n+1} - R^n\big) = \frac{R^{n+1}}{E(\bar{\boldsymbol{u}}_h^{n+1}) + C_0}(-\nu \|\nabla \bar{\boldsymbol{u}}_h^{n+1}\|^2 + (\boldsymbol{f}^{n+1}, \bar{\boldsymbol{u}}_h^{n+1})), \qquad (12b)\\
&\xi^{n+1} = \frac{R^{n+1}}{E(\bar{\boldsymbol{u}}_h^{n+1})}; \qquad (12c)\\
&\boldsymbol{u}_h^{n+1} = \eta_k^{n+1} \bar{\boldsymbol{u}}_h^{n+1} \ \text{ with } \eta_k^{n+1} = 1 - (1 - \xi^{n+1})^k, \qquad (12d)\\
&(\nabla p_h^{n+1}, \nabla q_h) = (\boldsymbol{f}^{n+1} - \boldsymbol{u}_h^{n+1} \cdot \nabla \boldsymbol{u}_h^{n+1} - 2\Omega^{n+1} \times \boldsymbol{u}_h^{n+1}, \nabla q_h) - \nu \int_{\partial D} (\nabla \times \boldsymbol{u}_h^{n+1} \times \nabla q_h) \cdot \boldsymbol{n} ds, \ \forall q_h \in Q_h. \qquad (12e)
\end{aligned}$$

- It is clear that the fully discrete scheme (12) admits a unique solution so it is well posed.
- There is strong numerical evidences (cf. [10,9]) that the pair $(\boldsymbol{X}_h, Q_h)$ does not need to satisfy the inf-sup condition for the pressure to have k-th order accuracy in time. Hence, we can use equal-order finite elements or spectral elements.

Since we shall consider a rectangular domain $D = (-1, 1)^d$ in our numerical simulations, we employ a Legendre-Galerkin method [27] for the spatial discretization. More precisely, let P_M be the space of polynomials of degree less than or equal to M, we set $X_h = P_M \cap H_0^1(D)$ and $M_h = P_M$ with $h = 1/M$. If $\hat{\boldsymbol{u}}_h^{n+1} = B_k(\boldsymbol{u}_h^n)$, i.e., the Coriolis force is treated explicitly, (12a) reduces to a set of decoupled Poisson type equation for each component of $\bar{\boldsymbol{u}}_h^{n+1}$ so it can be solved efficiently using a matrix diagonalization approach (cf. [27]). If $\hat{\boldsymbol{u}}_h^{n+1} = \bar{\boldsymbol{u}}_h^{n+1}$, all components of $\bar{\boldsymbol{u}}_h^{n+1}$ in (12a) are coupled so one has to solve the following coupled system at each time step:

$$\frac{\alpha_k}{\delta t}(\boldsymbol{u}_h, \boldsymbol{v}_h) + \nu(\nabla \boldsymbol{u}_h, \nabla \boldsymbol{v}_h) + 2(\Omega \times \boldsymbol{u}_h, \boldsymbol{v}_h) = (\boldsymbol{g}_h, v_h) \ \forall \boldsymbol{v}_h \in \boldsymbol{X}_h, \tag{13}$$

which can still be efficiently solved, with essentially the same computational cost as the decoupled case, by using a generalized diagonalization approach described in [2].

2.3. Stability proof

The unconditional stability of a similar scheme in the absence of $\boldsymbol{f}$ can be proved as in [14]. We now state and prove a stability result in the presence of the external force $\boldsymbol{f}$.

Theorem 1. *Let $\|\boldsymbol{f}(\cdot, t)\| \le C_{\boldsymbol{f}}, \quad \forall t \in [0, T]$, and $C_0 \ge \max\{2C_{\boldsymbol{f}}^2, 1\}$. Then, given $R^n > 0$, we have $R^{n+1} > 0$, $\xi^{n+1} > 0$ and there exists a constant M_T only depends on T such that*

$$\|\boldsymbol{u}^n\|, \ \|\boldsymbol{u}_h^n\| \le M_T, \quad \forall n \le T/\delta t, \tag{14}$$

where $\{\boldsymbol{u}^n\}$ and $\{\boldsymbol{u}_h^n\}$ are the solutions of the schemes (7) and (12), respectively.

Proof. The proof for the two schemes is essentially the same, so we shall only consider the scheme (7).
By the assumptions on $\boldsymbol{f}$ and C_0, we find

$$\Big|\frac{(\boldsymbol{f}^{n+1}, \bar{\boldsymbol{u}}^{n+1})}{E(\bar{\boldsymbol{u}}^{n+1}) + C_0}\Big| \le \frac{\|\boldsymbol{f}^{n+1}\| \, \|\bar{\boldsymbol{u}}^{n+1}\|}{E(\bar{\boldsymbol{u}}^{n+1}) + C_0} \le \frac{\|\boldsymbol{f}^{n+1}\| \, \|\bar{\boldsymbol{u}}^{n+1}\|}{\frac{1}{2}\|\bar{\boldsymbol{u}}^{n+1}\|^2 + 2\|\boldsymbol{f}^{n+1}\|^2} \le \frac{1}{2}. \tag{15}$$

Without loss of generality, we assume $\delta t \le 1$. Then, given $R^n > 0$, it follows from (7b) that

$$R^{n+1} = R^n \left(1 + \frac{\delta t \nu \|\nabla \bar{\boldsymbol{u}}^{n+1}\|^2}{E(\bar{u}^{n+1}) + C_0} - \frac{\delta t (\boldsymbol{f}^{n+1}, \bar{\boldsymbol{u}}^{n+1})}{E(\bar{\boldsymbol{u}}^{n+1}) + C_0}\right)^{-1} > 0. \tag{16}$$

Next, taking the sum of (7b) for n from 0 to m, using again (15), we obtain

$$\begin{aligned} R^{m+1} &= R^0 - \nu \delta t \sum_{j=0}^{m} \xi^{j+1} \|\nabla \bar{\boldsymbol{u}}^{j+1}\|^2 + \delta t \sum_{j=0}^{m} \xi^{j+1} (\boldsymbol{f}^{j+1}, \bar{\boldsymbol{u}}^{j+1}) \\ &\le R^0 + \delta t \sum_{j=0}^{m} \frac{R^{j+1}}{E(\bar{\boldsymbol{u}}^{j+1}) + C_0} (\boldsymbol{f}^{j+1}, \bar{\boldsymbol{u}}^{j+1}) \\ &\le R^0 + \delta t \sum_{j=0}^{m} \frac{\|\boldsymbol{f}^{j+1}\| \, \|\bar{u}^{j+1}\|}{E(\bar{\boldsymbol{u}}^{j+1}) + C_0} R^{j+1} \le R^0 + \frac{\delta t}{2} \sum_{j=0}^{m} R^{j+1}. \end{aligned}$$

Applying a discrete Gronwall lemma (see, for instance, Lemma B10 in [24]): to the above, we obtain

$$R^m \le C_T R^0, \quad \forall m \le T/\delta t,$$

which, along with $C_0 \ge 1$, implies that

$$|\xi^{n+1}| = \frac{R^{n+1}}{E(\bar{\boldsymbol{u}}^{n+1}) + C_0} \le \frac{2 C_T R^0}{\|\bar{\boldsymbol{u}}^{n+1}\|^2 + 2}. \tag{17}$$

Since $\eta^{n+1} = 1 - (1 - \xi^{n+1})^k$, we have $\eta^{n+1} = \xi^{n+1} P_{k-1}(\xi^{n+1})$ with P_{k-1} being a polynomial of degree $k-1$. Then, we derive from inequality (17) that there exists $M_T > 0$ such that

$$|\eta^{n+1}| = |\xi^{n+1} P_{k-1}(\xi^{n+1})| \le \frac{M_T}{\|\bar{\boldsymbol{u}}^{n+1}\|^2 + 2},$$

which, along with $\boldsymbol{u}^{n+1} = \eta^{n+1} \bar{\boldsymbol{u}}^{n+1}$, implies

$$\|\boldsymbol{u}^{n+1}\|^2 = (\eta^{n+1})^2 \|\bar{\boldsymbol{u}}^{n+1}\|^2 \le \left(\frac{M_T}{\|\bar{\boldsymbol{u}}^{n+1}\|^2 + 2}\right)^2 \|\bar{\boldsymbol{u}}^{n+1}\|^2 \le M_T^2. \quad \square$$

Remark 1. The above theorem only shows that the L^2-norm of the numerical solutions are uniformly bounded. In the space-periodic case, starting with a similar stability result, optimal error estimates are established [14] for the k-th ($1 \le k \le 5$) order SAV schemes. However, in the non-periodic case, error estimates of the above schemes are still elusive.

2.4. Accuracy tests

We now validate the scheme (12) with the Legendre-Galerkin approximation described above in the inertial range (i.e., $\Omega = 0$) with a manufactured analytical solution in $D \in (-1, 1)^2$ with $\nu = 0.01$:

$$\begin{aligned} u(x, y, t) &= \frac{1}{2} \cos^2(\frac{\pi x}{2}) \sin(\pi y) \sin(t), \\ v(x, y, t) &= -\frac{1}{2} \sin(\pi x) \cos^2(\frac{\pi y}{2}) \sin(t), \\ p(x, y, t) &= 10^4 \cos(\pi x) \sin(\pi y) \sin(t). \end{aligned}$$

The corresponding forcing term can be obtained from the equation (2a).

We set $C_0 = 100$, and choose $M = 20$ so that the spatial discretization error is negligible compared with the time discretization error. Fig. 1 (a) shows that the scheme (12) achieves the expected order of accuracy with $k = 2, 3, 4$.

3. Application to rotating fluids in a cube

In this section, we apply the scheme (12) with the Legendre-Galerkin approximation to study the dynamics of rotating fluid in a cube in three different scenarios, see Fig. 2. In all simulations below, we choose $C_0 = 10^4$.

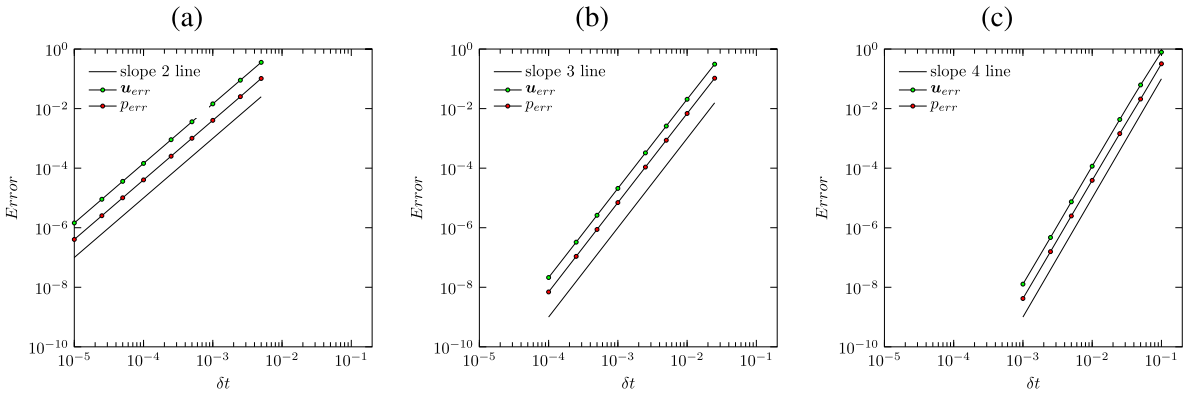

Fig. 1. (a) L^2-error plot of the 2nd-order SG-SAV scheme; (b) L^2-error plot of the 3rd-order SG-SAV scheme; (c) L^2-error plot of the 4th-order SG-SAV scheme.

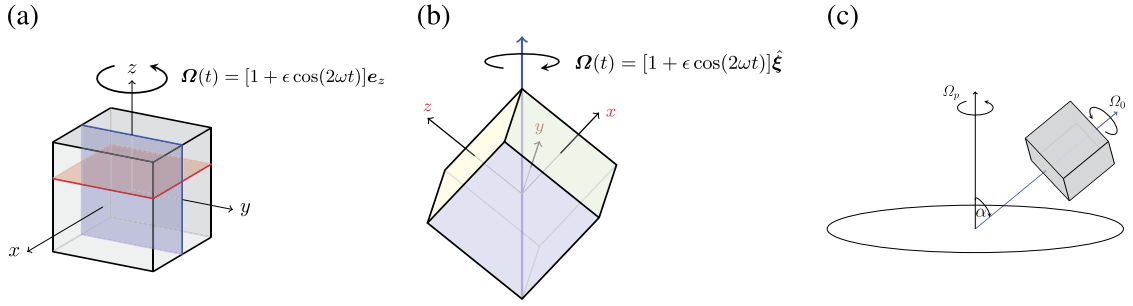

Fig. 2. (a) Schematic of the librating cube with rotation axis $\boldsymbol{e}_z = (0, 0, 1)$; (b) schematic of the librating cube with rotation axis $\hat{\boldsymbol{\xi}} = (1, 1, 1)/\sqrt{3}$; (c) schematic of the precessing cube with precessing angle $\alpha = 1$ degree.

3.1. A librating cube with rotation axis $\boldsymbol{e}_z = (0, 0, 1)$

A librating cube is a cube mounted on a constant rotating table with mean rotation angular velocity Ω_0. Meanwhile, the cube itself is modulated harmonically by an external forcing at a frequency 2ω and relative amplitude ϵ, which is often referred as the Rossby number of the libration, see Fig. 2(a), with the cube as the frame of reference, the non-dimensional governing equations are the Navier-Stokes equations (2) with the angular rotation velocity:

$$\boldsymbol{\Omega} = \Omega_0(1 + \epsilon\cos(2\omega\Omega_0 t))\boldsymbol{e}_z, \tag{19}$$

where $\boldsymbol{e}_z = (0, 0, 1)$. The boundary conditions for all velocity components are zero, and the phase of the librational forcing is defined as

$$\varphi = \mod(2\omega\Omega_0 t, 2\pi). \tag{20}$$

Let E_τ denote the strobe kinetic energy at forcing phase φ, and let $(\chi, \psi, \phi) = \nabla \times \boldsymbol{u}$ denote the vorticity field. The governing equations (2) with no-slip boundary conditions are invariant to a reflection through the plane $z = 0$ and a $\pi/2$ rotation about the z-axis. The actions of these symmetries on the velocity and pressure fields are

$$\mathcal{K}(u, v, w, p)(x, y, z, t) = (u, v, -w, p)(x, y, -z, t), \tag{21}$$

$$\mathcal{R}_{\pi/2}(u, v, w, p)(x, y, z, t) = (-v, u, w, p)(-y, x, z, t). \tag{22}$$

The flow responses consist of two main components: resonant excitation of inviscid inertial eigenmodes of the cube, and inertial wavebeams whose orientation is governed by the inviscid dispersion relation. When the ratio between external librational forcing frequency $2\omega\Omega_0$ and twice the background rotation frequency $2\Omega_0$ is $\omega \in [0, 1]$, the system will emanate inertial wavebeams from the edges where top and bottom walls meet each other due to the imbalance of flux on the surfaces of the cube. The angle θ formed by an inertial wavebeam and the plane orthogonal to the background rotation axis is determined by the dispersion relation [8]:

$$\cos(\theta) = 2\omega\Omega_0/(2\Omega_0) = \omega. \tag{23}$$

Table 1
The strobe kinetic energy E_τ of synchronized periodic DNS solutions at librational forcing phase $\varphi = 0$, $(\Omega_0, \epsilon) = (10^6, 10^{-6})$, and the half forcing frequency $\omega = 0.677$. The schemes, spatial resolutions M and number of time steps N per forcing period are indicated in the table. (x represents the solution blows up and NC represent the solution is not able to converge.)

M	2nd IPS			2nd SG-SAV-E			3rd SG-SAV-E			4th SG-SAV-E
	128	156	168	128	156	168	128	156	168	128
N=50	x	x	x	NC	NC	NC	0.0707	NC	NC	NC
N=100	0.0745	0.0745	0.0745	0.0745	0.0748	0.0746	0.0711	0.0711	0.0711	NC
N=200	0.0715	0.0715	0.0715	0.0715	0.0715	0.0715	0.0711	0.0711	0.0711	0.0711
N=400	0.0712	0.0712	0.0712	0.0712	0.0712	0.0712	0.0711	0.0711	0.0711	0.0711

Meanwhile, when the librational forcing frequency 2ω is close to the frequency 2σ of an inviscid inertial eigenmode preserving $\mathcal{K} \times \mathcal{R}_{\pi/2}$-symmetry, this particular eigenmode will be resonantly excited by the external librational forcing, which is both confirmed experimentally and numerically in [1] and [30]. In addition, the computation of intrinsic eigenmodes and eigen-frequencies with designated symmetries is presented in appendix A in [30].

This problem was initially studied through a physical experiment by [1], they conducted experiments at the background rotation rate $\Omega_0 = 2.65 \times 10^{4.7}$ with $\epsilon = 0.02$, and the half librational forcing frequency $\omega \in [0.60, 0.73]$. In addition, they found that roughly at the forcing frequency $\omega = 0.69$, the maximum energy was obtained under the external librational forcing. In order to better understand the physical mechanism of the flow dynamics inside a librating cube, a numerical investigation was conducted in [30] using a 2nd-order improved pseudo-spectral Chebyshev collocation method, hereafter referred as 2nd-order IPS scheme, which was proposed by [16]. The 2nd-order IPS scheme with explicit treatment of Coriolis force term is able to simulate the flow at background rotation rate as large as $\Omega_0 = 10^6$ with the modulation amplitude $\epsilon = 10^{-6}$, and the half forcing frequency ω from 0 to 1 with an increment 0.001. The challenges of simulating the flow at a very fast background rotation rate are: first, resolving the very thin boundary layers on each surface of the cube; second, the intense inertial wavebeams (shear layers) in the interior of the cube; third, the strong oscillations of excited eigenmodes of the cube while resonance occurs; fourth, large computational costs associated with increased resolution in space and time as there are several thousands cases need to be simulated. Therefore, a highly efficient and accurate numerical scheme is essential.

We first conduct a careful comparison between the 2nd-order IPS scheme and the SAV scheme with different-orders, all with explicit treatment of the Coriolis force. Note that the cost of the 2nd-order IPS scheme is roughly twice the cost of the SAV schemes, due to an extra step is used in the 2nd-order IPS scheme to update the velocity.

We simulate the librating flow at parameters $(\Omega_0, \epsilon) = (10^6, 10^{-6})$, and the half librational forcing frequency $\omega = 0.677$, which corresponds to the first low order eigenmode $M_{1.1}$ with the half frequency $\sigma_{1.1} = 0.6742$ (we adapt the notations used in [30]). The simulations are carried out at three different spatial resolutions $M = 128, 156, 168$ and four different numbers of time steps $N = 50, 100, 200, 400$ per librational forcing period for each single set of parameters $(\Omega_0, \epsilon, \omega)$. For each single case, we computed at least 2000 librational forcing periods, which grantees that the flow is fully synchronized with the external librational forcing. The results are displayed in Table 1, where N denotes the number of time steps per librational forcing period, i.e., the time step is given by

$$\delta t = \pi / (N \omega \Omega_0) \tag{24}$$

Due to the very small modulation amplitude $\epsilon = 10^{-6}$, the steady state solutions are limit cycles with periods the same as the librational forcing. The flow is quantified by the strobe kinetic energy E_τ at each forcing period. For instance, when the flow is synchronized with a particular forcing frequency, then the strobe kinetic energy E_τ at each forcing period should be a constant.

Table 1 shows the strobe kinetic energy E_τ by different schemes with different discretization parameters. In Table 1 and hereafter, x means that the numerical scheme blows up, NC means that numerical solution failed to produce a converged synchronized periodic solution, and SG-SAV-E means the Spectral-Galerkin SAV scheme with explicit treatment of the Coriolis force.

We observe that for each fixed number of time steps N, $M = 128, 156, 168$ lead to essentially the same result which indicates that $M = 128$ is sufficient for spatial resolution.

- For the 2nd-order IPS scheme, when $N = 50$ time steps per forcing period, the solution blows up, and it can lead to a decent converged synchronized periodic solution with $N = 400$.
- The accuracy of the 2nd-order SG-SAV-E scheme is similar to 2nd-order IPS scheme, although it does not blow up with $N = 50$, as the SAV approach is always stable, but it does not lead to meaningful result with $N = 50$.
- The 3rd-order SG-SAV-E scheme leads to a reasonable result with $N = 50$ and a very accurate result with $N = 100$, while fourth SG-SAV-E scheme requires $N = 200$ to produce an accurate result.
- In order to make a visual comparison, we plot in Fig. 3 the snapshots of the x-component vorticity χ in the plane $x = 0$, and in Fig. 4 z-component vorticity ψ in the plane $z = 0$ at the librational forcing phase $\varphi = \pi/2$ with different schemes. We observe that with $N = 100$, the results by both second-order schemes are qualitative different from those

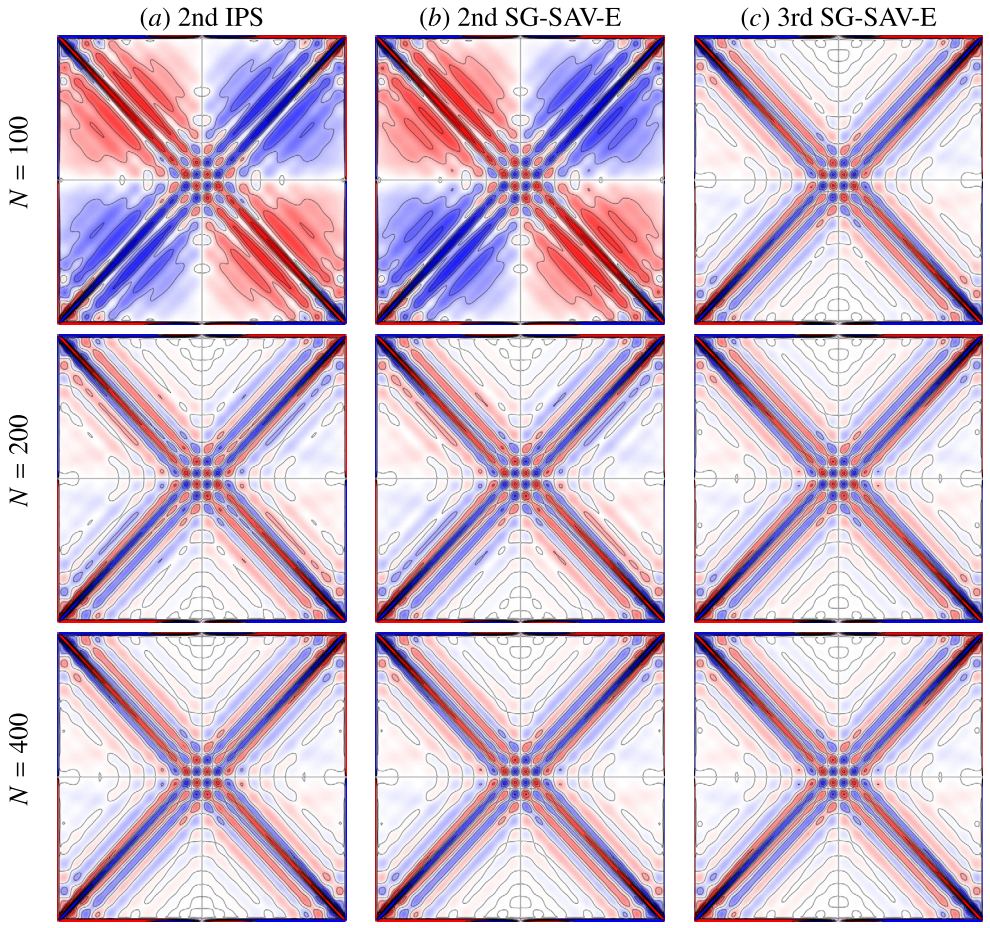

Fig. 3. Contours of x-component vorticity χ in the vertical plane $x = 0$ at phase $\varphi = \pi/2$, $(\Omega_0, \epsilon, \omega) = (10^6, 10^{-6}, 0.677)$. The contour levels are equally spaced in $[-2.5, 2.5]$ and the colormap is consistent with the contour levels. The DNS solutions are obtained by using $M = 156$ basis functions in each coordinate direction. The numerical schemes and the number of time steps N per forcing period are indicated in the table. Each snapshot is plotted on the 201 by 201 uniform grids using spectral interpolation.

with $N = 400$, while the 3rd-order SG-SAV-E scheme with $N = 100$ leads to very accurate result. These are consistent with Table 1. Moreover, we observe from Fig. 4 that even at $N = 400$, the result obtained by the 2nd-order IPS scheme has visibly difference in the center with those by thee SAV schemes.

To summarize, the above results indicate that for this example, (i) the 2nd-order SG-SAV-E scheme has better stability and slightly better accuracy than the 2nd-order IPS scheme; (ii) the 4th-order SG-SAV-E scheme requires smaller time steps to obtain accurate results; (iii) the 3rd-order SG-SAV-E scheme is the most efficient in terms of the cost/accuracy ratio.

3.2. A librating cube with rotation axis $\hat{\boldsymbol{\xi}} = (1, 1, 1)/\sqrt{3}$

The configuration of this problem is essentially the same as that of Subsection 3.1, the only difference is that the rotation axis is the diagonal line pointing at the direction $\hat{\boldsymbol{\xi}} = (1, 1, 1)/\sqrt{3}$, see Fig. 2(b). The corresponding angular velocity vector is:

$$\boldsymbol{\Omega} = \Omega_0(1 + \epsilon \cos(2\omega\Omega_0 t))\hat{\boldsymbol{\xi}}. \tag{25}$$

The governing equations (2) and boundary conditions are invariant to a discrete rotation $\mathcal{R}_{2\pi/3}$ of angle $2\pi/3$ about the rotation axis $\boldsymbol{\xi}$ and a reflection through the origin C. The actions of these two symmetries on the velocity and pressure fields are

$$\mathcal{R}_{2\pi/3} : [u, v, w, p](x, y, z, t) \mapsto [w, u, v, p](z, x, y, t), \tag{26}$$

$$C : [u, v, w, p](x, y, z, t) \mapsto [-u, -v, -w, p](-x, -y, -z, t). \tag{27}$$

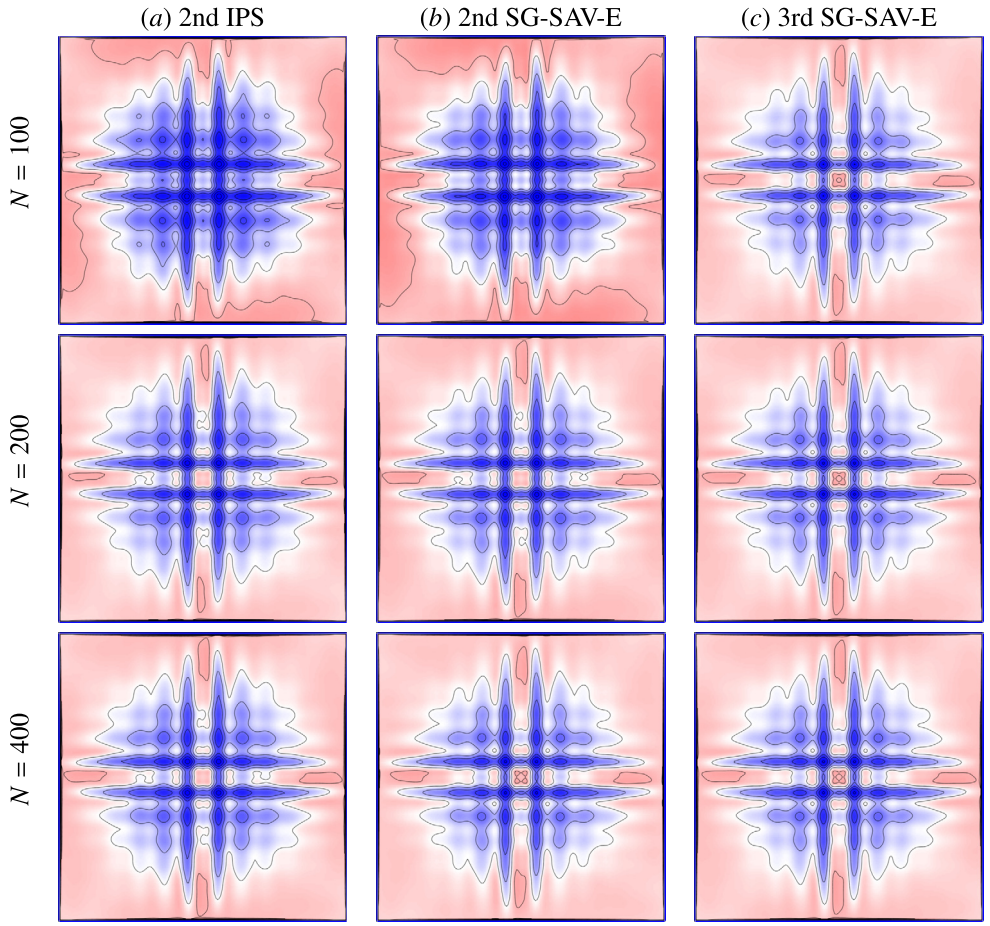

Fig. 4. Contours of z-component vorticity ψ in the horizontal plane $z = 0$ at phase $\varphi = 0$, $(\Omega_0, \epsilon, \omega) = (10^6, 10^{-6}, 0.677)$. The contour levels are equally spaced in $[-4, 4]$ and the colormap is consistent with the contour levels. The DNS solutions are obtained by using $M = 156$ basis functions in each coordinate direction. The numerical schemes and the number of time steps N per forcing period as indicated. Each snapshot is plotted on the 201 by 201 uniform grids using spectral interpolation.

The time evolution of the flow responses is quantified by the strobe kinetic energy E_τ at the librational forcing phase $\varphi = 0$. The visualization quantity used here is the enstrophy $\mathcal{E}$, which is defined as

$$\mathcal{E} = |\nabla \times \boldsymbol{u}|^2 \tag{28}$$

Unlike the case in Subsection 3.1, the rotation axis $\boldsymbol{e}_z = (0, 0, 1)$ is either parallel or orthogonal to the faces of the cube. With rotation axis $\hat{\boldsymbol{\xi}} = (1, 1, 1)/\sqrt{3}$, which is neither parallel nor orthogonal the faces of the cube, the system only supports inertial wavebeams. A detailed numerical investigation of this problem for the background rotation as large as $\Omega_0 = 10^7$ with modulation amplitude $\epsilon = 10^{-7}$ is carried out using the 2nd-order IPS scheme in [32]. It is found that at very low frequencies, the 2nd-order IPS scheme requires a very large number of time steps per forcing period. For instance, at the parameter set $(\Omega_0, \epsilon, \omega) = (10^7, 10^{-7}, 0.05)$, it requires at least $N = 1200$ time steps per forcing period to obtain a synchronized periodic solution. In addition, when the background rotation rate further increased to $\Omega_0 = 10^8$ with $\epsilon = 10^{-8}$, the 2nd-order IPS scheme failed to obtain any meaningful solutions.

We first conduct the simulation at the same parameter set $(\Omega_0, \epsilon, \omega) = (10^7, 10^{-7}, 0.05)$, spatial resolution $M = 200$ using the 3rd SG-SAV-E scheme to validate the results. We observe from Fig. 5 that the 3rd-order SG-SAV-E is able to obtain a synchronized converged periodic solution using $N = 200$ time steps per forcing period with the strobe kinetic energy $E_\tau = 0.0863$ at the same forcing phase. The results are also visually identical to those obtained with the 2nd-order IPS scheme using $N = 1200$ time steps per forcing period with the strobe kinetic energy $E_\tau = 0.0863$.

Then we use the 3rd-order SG-SAV-E scheme to simulate the background rotation rate $\Omega_0 = 10^8$ with the modulation amplitude $\epsilon = 10^{-8}$, a case which the 2nd-order IPS scheme failed to obtain a convergent solution. The results are plotted in Fig. 6. Qualitatively, the structure of enstrophy is similar as in Fig. 5, but with much stronger intensity of the inertial wavebeams due to the background rotation rate is one order of magnitude higher. The contours of the three plots are smooth,

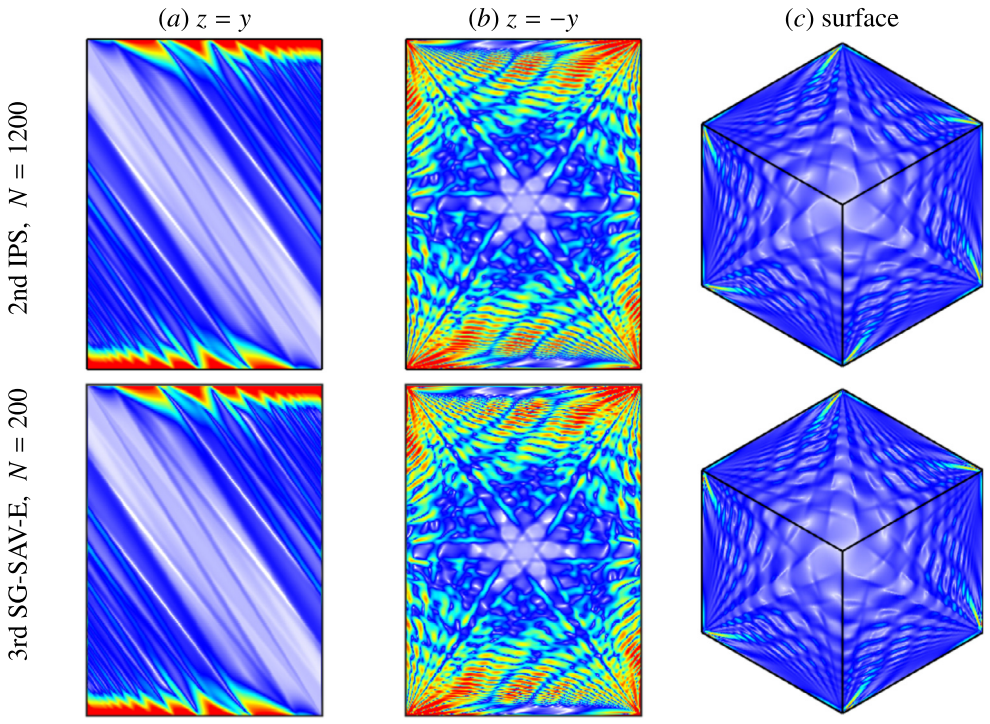

Fig. 5. Contours of scaled enstrophy $\log_{10}(\mathcal{E})$ in the diagonal planes (*a*) $z = y$, (*b*) $z = -y$, and scaled enstrophy $\mathcal{E}^{1/4}$ on the surfaces (*c*) at librational forcing phase $\varphi = 0$, $(\Omega_0, \epsilon, \omega) = (10^7, 10^{-7}, 0.05)$. The contour levels for (*a*), (*b*) are equally spaced in $[0, 4]$, and the contour levels for (*c*) are equally spaced in $[0, 100]$. The DNS solutions are obtained using $M = 200$ basis functions in each coordinate direction, and the schemes and the number of time steps N per forcing period are indicated in the figure. Each snapshot is plotted on the 501 by 501 uniform grids using spectral interpolation.

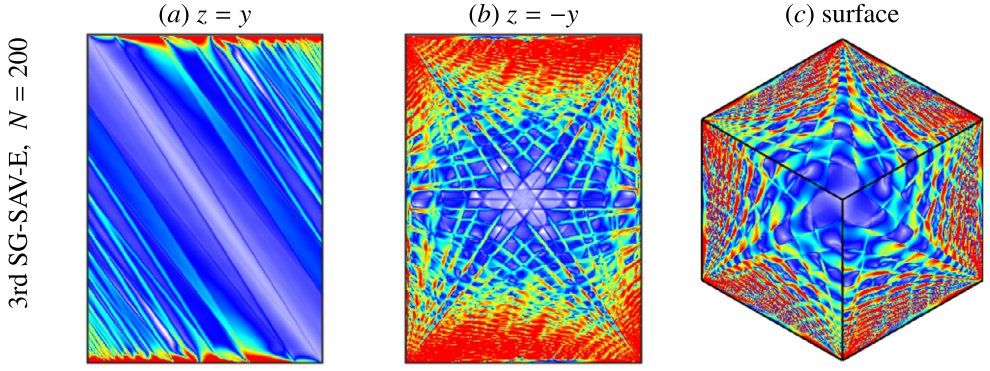

Fig. 6. Contours of scaled enstrophy $\log_{10}(\mathcal{E})$ in the diagonal planes (*a*) $z = y$, (*b*) $z = -y$, and scaled enstrophy $\mathcal{E}^{1/4}$ on the surfaces (*c*) at librational forcing phase $\varphi = 0$, $(\Omega_0, \epsilon, \omega) = (10^8, 10^{-8}, 0.05)$. The contour levels for (*a*), (*b*) are equally spaced in $[0, 4]$, and the contour levels for (*c*) are equally spaced in $[0, 100]$. The DNS solution is obtained using $M = 350$ basis functions in each coordinate direction, and the scheme and the number of time steps N per forcing period are indicated in the figure. Each snapshot is plotted on the 501 by 501 uniform grids using spectral interpolation.

which indicate that the numerical solution is well resolved. This example demonstrates the robustness of the proposed 3rd-order SG-SAV-E scheme, which allows us to conduct simulations in a much wide wider range in the parameter-space.

3.3. A precessing cube

In the previous two examples, we only considered SAV schemes with explicit treatment of the Coriolis force. We now examine the effectiveness of SAV schemes with implicit treatment of the Coriolis force. We consider a cube mounted at the center of a horizontal rotating table with constant angular velocity Ω_p pointing in the vertical direction, and the cube itself rotates with a constant angular velocity Ω_0 about its axis. The cube axis is tilted an angle $\alpha = 1^\circ$ relative to the vertical axis and is at rest relative to the rotating table, see Fig. 2(c). In geophysical fluid dynamics, Ω_p and α are termed as the precessing angular velocity and precessing angle respectively. Using Cartesian coordinates $\boldsymbol{r} = (x, y, z)$ in the non-inertial

Table 2
The strobe kinetic energy E_τ of synchronized periodic solutions at precessional forcing phase $\varphi = \pi/2$, $(\Omega_0, \omega) = (4 \times 10^5, 0.507)$ and the schemes, spatial resolutions M and the number of time steps N per forcing period are indicated in the table.

M	2nd IPS	2nd SG-E	2nd SG-SAV-E	3rd SG-I	3rd SG-SAV-I
	128	128	128	128	128
N=100	x	x	2008	2181	1937
N=200	2001	2007	1992	1961	1934
N=400	1952	1953	1951	1936	1934
N=800	1938	1938	1938	1934	1934

frame of reference attached to the cube with the z axis aligned with the precession axis and the origin at the center of the rotating table, the governing equations are still (2) and the boundary conditions are zero. The corresponding angular velocity is:

$$\boldsymbol{\Omega} = \langle \Omega_p \sin(\alpha)\cos(\Omega_0 t), \Omega_p \sin(\alpha)\sin(\Omega_0 t), \Omega_0 + \Omega_p \cos(\alpha) \rangle \tag{29}$$

The Reynolds number Re, Poincare number Po, precessing amplitude a and precessing frequency 2ω can be defined as:

$$\begin{aligned} Po &= \Omega_p/\Omega_0 \\ Re &= \Omega_0 + \Omega_p \cos(\alpha) \\ a &= |Po| \sin(\alpha) \\ 2\omega &= \Omega_0/Re \end{aligned} \tag{30}$$

Similar to the librating cube, when the ratio between the precessing rate Ω_0 and twice the mean background rotation rate $2Re$ is $\omega \in [0, 1]$, the system will emit inertial wavebeams oblique to the rotation axis from the edges where vertical wall meets with horizontal walls. The angle β formed between the wave vector of a particular wavebeam and the plane orthogonal to the mean rotation axis (z axis in the cube reference) is determined by the dispersion relation:

$$\cos(\beta) = \omega \tag{31}$$

On the other hand, when the precessional forcing frequency close to one of the frequencies of intrinsic eigenmodes which preserve the two space-time symmetries: $\mathcal{T}_{\tau/2}\mathcal{K}$, a reflection about the axial midplane together with a half-period translation in time; $\mathcal{T}_{\tau/4}\mathcal{R}_{\pi/2}$, a quarter rotation about the axis together with a quarter period translation time where $\tau = \pi/\omega$ is the period of the precessional forcing. The flip symmetry $\mathcal{K}$ about $z = 0$ and the $\pi/2$ rotational symmetry about the mean rotation axis are defined in (21) and (22) respectively. The time translation $\mathcal{T}_\rho$ is defined as:

$$\mathcal{T}_\rho(u, v, w)(x, y, z, t) = (u, v, w)(x, y, z, t + \rho), \text{ for arbitrary } \rho. \tag{32}$$

The two space-time symmetries are the fundamental symmetries of the system, and they combine into a purely spatial centro-symmetry C, which is defined as:

$$C(u, v, w)(x, y, z, t) = (-u, -v, -w)(-x, -y, -z, t). \tag{33}$$

The centro-symmetry will be used to track the time evolution of DNS solutions, especially when the system breaks the two fundamental symmetries. The centro-symmetry factor is defined as

$$\mathcal{S} = \|C(\boldsymbol{u}) - \boldsymbol{u}\|/\|\boldsymbol{u}\| \tag{34}$$

This problem was initially investigated by [6] and [7] numerically using a finite difference scheme with slip boundary conditions to study the dynamo mechanism in a precessing cube. They used slip boundary conditions for the velocity fields and were only able to conduct the simulations for the Ekman number ranges from 10^{-3} to 10^{-5} due to the computational cost. Later a more detailed numerical study was conducted by [31] using the 2nd-order IPS scheme, in which the excitation of the intrinsic eigenmodes of the cube and the dynamical process of the emergence of triadic resonance is captured. In addition, the modes with different space-time symmetries are also identified.

3.3.1. Synchronized periodic solutions: excitation of intrinsic eigenmodes of the cube

In Table 2, we list the strobe kinetic energy E_τ of synchronized periodic solutions at the precessional forcing phase $\varphi = \pi/2$, $(\Omega_0, \omega) = (4 \times 10^5, 0.507)$, and spatial resolution $M = 128$ obtained by different schemes. In the table, SG-E (resp. SG-I) means spectral-Galerkin method with explicit (resp. implicit) treatment of the Coriolis force.

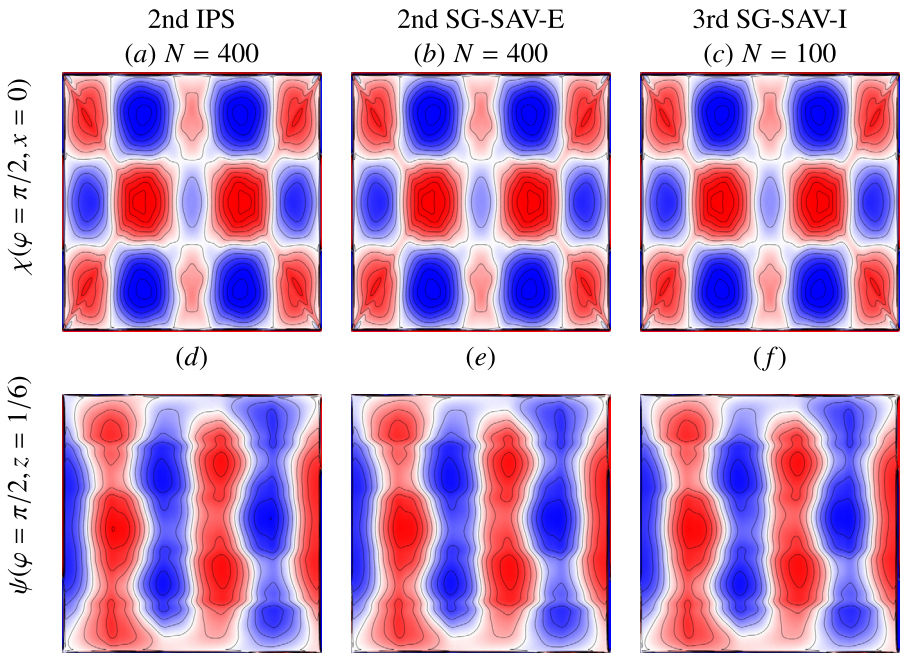

Fig. 7. Contours of (top row) x-component vorticity χ in the vertical plane $x = 0$ and contours of (bottom row) z-component vorticity ψ in the horizontal plane $z = 1/6$ at precessional forcing phase $\varphi = \pi/2$, $(\Omega_0, \omega) = (4 \times 10^5, 0.507)$ obtained by different schemes as indicated. The contour levels are equally spaced in $[-2.5, 2.5] \times 10^3$ and the colormap is consistent with the contour levels. The DNS solutions are obtained using $M = 128$ basis functions in each coordinate direction. The schemes and the number of time steps N per forcing period are indicated in the figure. Each snapshot is plotted on the 201 by 201 uniform grids using spectral interpolation.

On the other hand, some visual comparisons are presented in Fig. 7. We observe no visual difference between the results obtained by the 3rd-order SG-SAV-I scheme with $N = 100$ time steps and the 2nd-order schemes with $N = 400$ time steps.

Hence, for this example, the following observations can be made:

- The three second-order schemes require $N = 800$ to obtain a reasonably accurate solution, the 2nd-order SG-SAV-E performs the best among the three schemes.
- The 3rd-order SG-I scheme is much better than all second-order schemes. However, it still requires $N = 400$ to obtain an accurate solution, and $N = 800$ to obtain a very accurate solution.
- The 3rd-order SG-SAV-I scheme performs the best among all schemes, requiring only $N = 100$ to obtain an accurate solution and $N = 200$ to obtain a very accurate solution.

The above observations indicate that combining SAV, third-order and implicit treatment of the Coriolis force can greatly improve the efficiency and accuracy.

3.3.2. The functionality of SAV factor

The SAV factor ξ^{n+1} plays a delicate role in balancing stability and accuracy. In order to articulate the functionality of the SAV factor ξ^{n+1}, we compare the solutions at the same parameter set $(\Omega_0, \omega) = (4 \times 10^5, 0.507)$, space resolution $M = 128$, and initial conditions zero obtained by the proposed SAV schemes and the corresponding semi-implicit schemes, i.e., setting $\eta^{n+1} = 1$ in the SAV schemes. In Fig. 8(a), we plot the temporal evolutions of the strobe kinetic energy E_τ obtained by the 2nd-order SG-SAV-E and 2nd-order SG-E schemes. We observe that without using SAV, the strobe kinetic energy E_τ (the blue dashed curve), grows exponentially after roughly 1200 forcing periods and eventually blows up. On the contrary, the strobe kinetic energy E_τ (the red solid curve) obtained by the 2nd-order SG-SAV-E scheme stays bounded all time. We plot in Fig. 8(b) the evolution of the SAV factor ξ^{n+1}, and we observe that ξ^{n+1} remains close but less than 1, which effectively stabilizes the numerical solution while preserves a reasonable accuracy.

3.3.3. Symmetry breaking solutions: triadic resonance

With small precessional forcing, the flow is periodic and preserves the two fundamental space-time symmetries: $\mathcal{T}_{\tau/2}\mathcal{K}$, and $\mathcal{T}_{\tau/4}\mathcal{R}_{\pi/2}$. As the precessional forcing becomes stronger, e.g. increasing the precessional forcing amplitude, not only the intrinsic eigenmodes with the two space-time symmetries will be resonantly excited, but also the eigenmodes with other space-time symmetries would be excited too and triadic resonance occurs. Triadic resonance means that there are three different eigenmodes with different symmetries resonantly excited at the same time along with the breaking of the fundamental symmetries of the system. It has been identified that at the background rotation rate $\Omega_0 = 5.8 \times 10^4$ and half

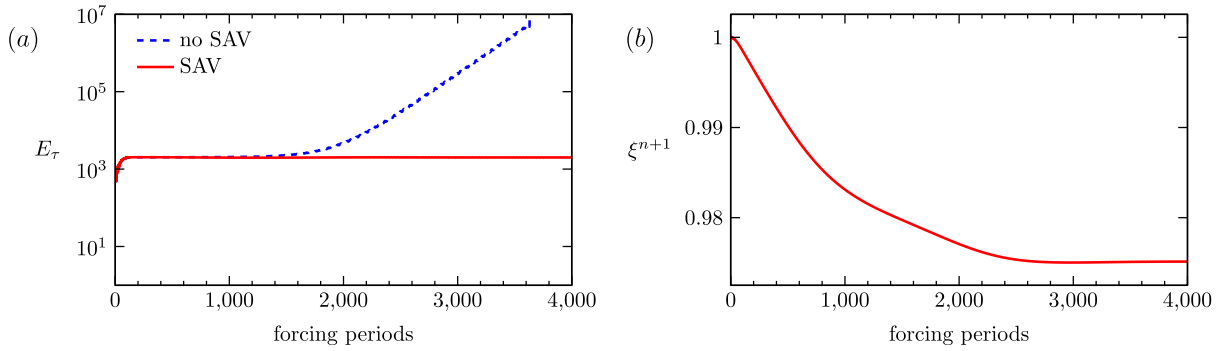

Fig. 8. Temporal evolutions of (*a*) strobe kinetic energy E_τ and (*b*) the SAV factor ξ^{n+1} at $(\Omega_0, \omega) = (4 \times 10^5, 0.507)$, spatial resolution $M = 128$, and $N = 100$ time steps per forcing period with the initial conditions zero. (For interpretation of the colors in the figure(s), the reader is referred to the web version of this article.)

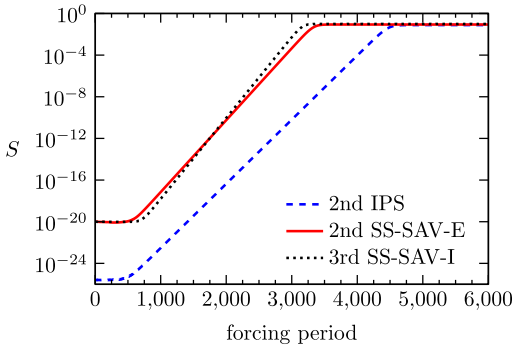

Fig. 9. Temporal evolutions of (*a*) the strobe centro-symmetry factor S and (*b*) the strobe total kinetic energy E_τ at the rotation rate $\Omega_0 = 5.8 \cdot 10^4$ and half precessional forcing frequency $\omega = 0.346 (Po = 0.444)$ obtained by different schemes as indicated. The DNS solutions are obtained by using the same synchronized periodic solution at $\Omega_0 = 5.6 \cdot 10^4$ and half precessional forcing frequency $\omega = 0.346$ as the initial condition, $M = 96$ basis functions in each coordinate direction, and $N = 200$ time steps per precessional forcing period.

precessional forcing frequency $\omega = 0.346\,(Po = 0.444)$, the flow becomes quasi-periodic and triadic resonance occurs. The three modes are: the dominant one $\mathrm{M}^+_{1.1}$, which has the two fundamental symmetries $\mathcal{T}_{\tau/2}\mathcal{K}$ and $\mathcal{T}_{\tau/2}\mathcal{R}_{\pi/2}$ symmetries; the secondary mode $\mathrm{M}^-_{2.18}$, which has $\mathcal{K}$ and $\mathcal{T}_{-\tau/2}\mathcal{R}_{\pi/2}$ symmetries; the last mode is $\mathrm{M}^-_{1.1}$, which has $\mathcal{T}_{\tau/2}\mathcal{K}$ and $\mathcal{T}_{-\tau/2}\mathcal{R}_{\pi/2}$ symmetries (more details can be found in section 7 triadic resonance of [31]).

Next, we present simulations using the proposed SAV schemes to reproduce the dynamical process from the synchronized periodic solution to the triadic resonate quasi-periodic solution.

At $\Omega_0 = 5.6 \times 10^4$ and half precessing frequency $\omega = 0.346$, spatial resolution $M = 96$, and $N = 200$ time steps per forcing period, the 2nd-order IPS, 2nd-order SG-SAV-E and 3rd SG-SAV-I schemes all obtain the same stable synchronized periodic solutions. We use these stable solutions as the initial conditions, and increase the background rotation rate to $\Omega_0 = 5.8 \times 10^4$, while keeping all other parameters the same. The time evolution of the flow dynamics is tracked via the strobe centro-symmetry factor $\mathcal{S}$ defined in (34).

Fig. 9 shows the temporal evolutions of the strobe centro-symmetry factor $\mathcal{S}$ obtained by different schemes. Initially the symmetry factor $\mathcal{S}$ is close to machine epsilon. Roughly after 500 forcing periods, the blue dashed curve by the 2nd-order IPS scheme starts to increase exponentially, which implies the system starts to break the centro-symmetry as a consequence of breaking the two fundamental space-time symmetries: $\mathcal{T}_{\tau/2}\mathcal{K}$ and $\mathcal{T}_{-\tau/2}\mathcal{R}_{\pi/2}$, due to the excitation of intrinsic eigenmodes with different symmetries. After 4500 forcing periods, the blue dashed curve by the 2nd-order IPS scheme stops increasing and becomes flat, which implies the flow is fully stabilized and the centro-symmetry factor $\mathcal{S}$ is roughly 0.7. The temporal evolution of the strobe centro-symmetry factor $\mathcal{S}$ illustrated in Fig. 9 obtained by 2nd-order IPS scheme quantitatively demonstrates the dynamics process of emergence of the triadic resonance.

We observe from Fig. 9 that both SAV schemes capture the dynamical process of the triadic resonance, and the strobe centro-symmetry factors are all consistent with that of obtained by 2nd-order IPS scheme, but *they take a much smaller number of forcing periods to reach the stabilized state of the triadic resonance.*

Finally, we perform simulations using different schemes to reveal the structures of the eigenmodes of the identified triadic resonance, further validating the accuracy and efficiency of the SAV schemes.

We know the three eigenmodes are $\mathrm{M}^+_{1.1}$, $\mathrm{M}^-_{2.18}$ and $\mathrm{M}^-_{1.1}$. At the horizontal plane $z = 0$, the contributions of the eigenmodes $\mathrm{M}^+_{1.1}$ and $\mathrm{M}^-_{1.1}$ for z-component vorticity ψ are 0, and at the horizontal plane $z = 0.25$, the contribution of the modes

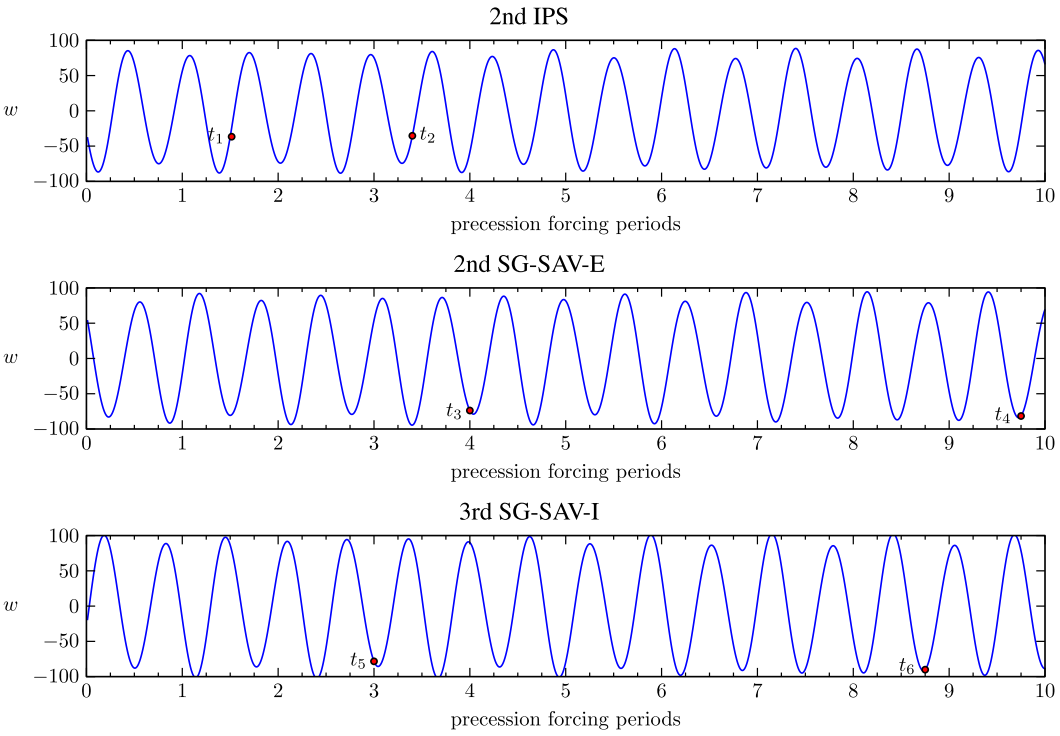

Fig. 10. Time series of the z-component of velocity w at the collocation grid point $(x, y, z) = (0, 0, 0)$ for $\Omega_0 = 5.8 \times 10^4$ and half forcing frequency $\omega = 0.343$. The symbols labeled t_1 through t_6 corresponds to the times where snapshots of the flow are shown in Fig. 11 and Fig. 12.

$M^-_{2,18}$ for z-component vorticity ψ is 0. In addition, at the different time instants, in the vertical plane $x = 0$, the structures of different eigenmodes can be distinguished too. Using the stabilized DNS solutions at 6000 forcing periods in Fig. 9 as initial conditions, let the flow responses further evolve 10 forcing periods, we plot in Fig. 10 the temporal evolutions of z-component velocity ψ at the physical space $(x, y, z) = (0, 0, 0)$ obtained by different schemes.

Then, we plot in Fig. 11 snapshots of x-component vorticity in the vertical plane $x = 0$ and z-component vorticity in the horizontal planes $z = 0$ obtained by different schemes at the time instants t_1, t_3, t_5 labeled in Fig. 10. Clearly, at the chosen time instants, the x-component vorticity χ in the vertical plane $x = 0$ shows the structure of x-component vorticity of the eigenmode $M^-_{2,18}$. Qualitatively, the snapshots of x-component vorticity obtained by different schemes are all similar to each other, which is characterized by two cells line up in the vertical z direction with opposite signs and nine cells line up in the horizontal y direction with alternating signs of neighboring cells. At the horizontal plane $z = 0$, due to the fact that the contribution of the z-component vorticity ψ from eigenmodes $M^+_{1,1}$ and $M^-_{1,1}$ is zero, the z-component of the vorticity ψ of eigenmode $M^-_{2,18}$, characterized by two strong small cells with alternating signs lie in the center of the plane and surrounded by multiple small cells, is well captured at these chosen times. Therefore the existence of eigenmode $M^-_{2,18}$ is identified visually.

We also plot in Fig. 12 snapshots of vorticity fields on the indicated planes at time instants t_2, t_4, t_6 labeled in Fig. 9. At the chosen time instants, in the vertical plane $x = 0$, the snapshots illustrate the structure of the x-component vorticity fields of the eigenmode $M^+_{1,1}$, which is characterized by three cells with alternating signs line up in the y-coordinate direction. In the horizontal plane $z = 0.25$, the snapshots illustrate the structure of the z-component vorticity fields of the eigenmode $M^+_{1,1}$ due to it is the dominate one, which is characterized by two large cells with opposite signs in the center of the plane. At the chosen time instants, the vorticity components in the plane $x = 0$ and $z = 0.25$ confirms the existence of the eigenmode $M^+_{1,1}$.

4. Concluding remarks

We constructed a new class of time discretization schemes for the Navier-Stokes equations with non-periodic boundary conditions by combining the SAV approach for general dissipative systems in [15] and the consistent splitting schemes in [10], and validated the new schemes by simulating a series of highly complex geophysical flows.

Our main contributions are:

- The new class of SAV schemes are unconditionally stable, only require solving linear equations with constant coefficients at each time step, and can be up to six-order accurate in time.

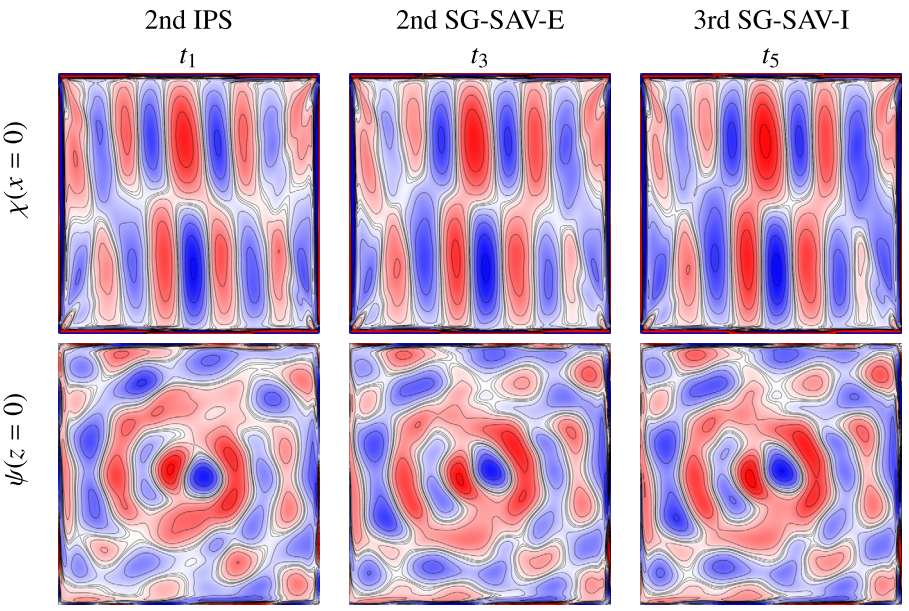

Fig. 11. Snapshots of x-component vorticity χ and z-component vorticity ψ in the indicated planes at $(\Omega_0, \omega) = (5.8 \times 10^4,\ \omega = 0.346)$ and the time instants t_1, t_3, t_5 corresponding to the red symbols in the time series obtained by different schemes in Fig. 10. DNS solutions are plotted in the uniformly 201 by 201 grid points through spectral interpolation, and all the contour levels are equally spaced in $[-2.2, 2.2] \times 10^4$, and the colormap is consistent with the contour levels.

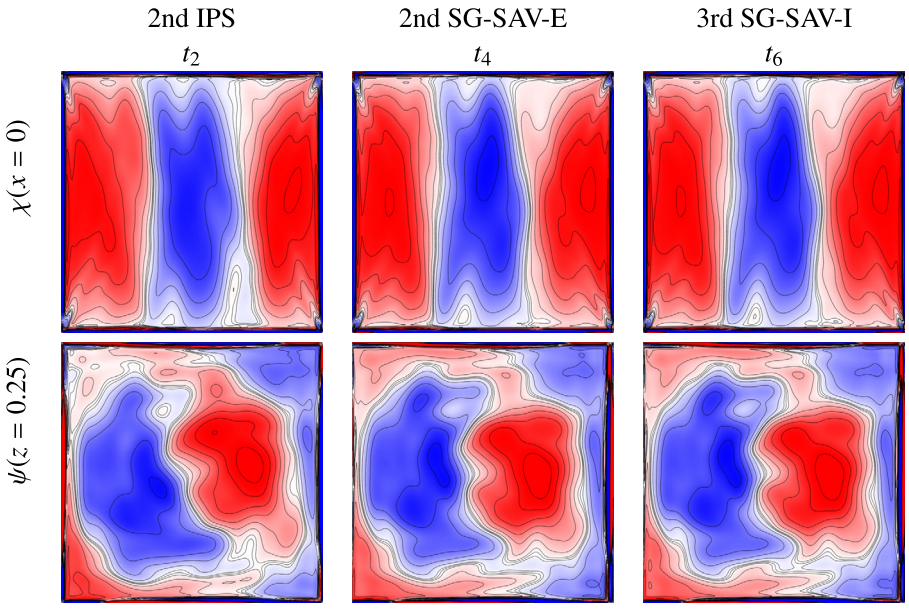

Fig. 12. Snapshots of x-component vorticity χ and z-component vorticity ψ in the indicated planes at $(\Omega_0, \omega) = (5.8 \times 10^4,\ \omega = 0.346)$ and the time instants t_2, t_4, t_6 corresponding to the red symbols in the time series obtained by different schemes in Fig. 10. DNS solutions are plotted in the uniformly 201 by 201 grid points through Legendre spectral interpolation, and all the contour levels are equally spaced in $[-2.2, 2.2] \times 10^4$, and the colormap is consistent with the contour levels.

- We validated the new class of SAV schemes by simulating rotating flows with highly complex spatial-temporal structures, demonstrated advantages of the new SAV schemes compared with usual semi-implicit schemes.
- By using a Legendre-Galerkin method in space which can treat the Coriolis force implicitly with essentially the same computational cost as treating the Coriolis force explicitly, we were able to simulate the rotating flows at the Ekman number $E = 10^{-8}$ with relatively large time steps, which is an order of magnitude smaller than the current available results.

For the parameter ranges considered in this paper, it is found that the 3rd-order SAV schemes are the most efficient in terms of accuracy vs. computational cost, and the fourth-order SAV schemes require smaller time steps to obtain meaningful solutions. It can be speculated that when the flows become even more complex in time and space as we decrease further the Ekman number, the fourth or even higher-order SAV schemes would outperform the third-order SAV schemes.

We only considered the Navier-Stokes equations in this paper. However, the new SAV schemes that we constructed here can be coupled with the SAV approach for general dissipative systems to construct higher-order and decoupled schemes for other complex nonlinear systems such as the Navier-Stokes Cahn-Hilliard system for two-phase flows.

CRediT authorship contribution statement

Ke Wu, Fukeng Huang and Jie Shen all contributed to the conceptualization, methodology and writing. Ke Wu carried out most of the numerical simulations.

Declaration of competing interest

The authors declare that they have no known competing financial interests or personal relationships that could have appeared to influence the work reported in this paper.

References

[1] J. Boisson, C.M. Lamriben, L.R. Mass, P.P. Cortet, F. Moisy, Inertial waves and modes excited by the libration of a rotating cube, Phys. Fluids 24 (2012) 076602.
[2] Feng Chen, Jie Shen, Efficient spectral-Galerkin methods for systems of coupled second-order equations and their applications, J. Comput. Phys. 231 (15) (2012) 5016–5028.
[3] Alexandre Joel Chorin, Numerical solution of the Navier-Stokes equations, Math. Comput. 22 (1968) 745–762.
[4] Michel O. Deville, Paul F. Fischer, E.H. Fischer, et al., High-Order Methods for Incompressible Fluid Flow, vol. 9, Cambridge University Press, 2002.
[5] Roland Glowinski, Finite element methods for incompressible viscous flow, Handb. Numer. Anal. 9 (2003) 3–1176.
[6] O. Goepfert, A. Tilgner, Dynamos in precessing cubes, New J. Phys. 18 (2016) 103019.
[7] O. Goepfert, A. Tilgner, Mechanisms for magnetic field generation in precessing cubes, Geophys. Astrophys. Fluid Dyn. 113 (1–2) (2019) 222–234.
[8] H.P. Greenspan, The Theory of Rotating Fluids, Cambridge Univ. Press, 1968.
[9] J.L. Guermond, P. Minev, Jie Shen, An overview of projection methods for incompressible flows, Comput. Methods Appl. Mech. Eng. 195 (44–47) (2006) 6011–6045.
[10] J.L. Guermond, Jie Shen, A new class of truly consistent splitting schemes for incompressible flows, J. Comput. Phys. 192 (1) (2003) 262–276.
[11] J.L. Guermond, Jie Shen, Velocity-correction projection methods for incompressible flows, SIAM J. Numer. Anal. 41 (1) (2003) 112–134.
[12] Jean-Luc Guermond, Peter Minev, High-order time stepping for the incompressible Navier-Stokes equations, SIAM J. Sci. Comput. 37 (6) (2015) A2656–A2681.
[13] Max D. Gunzburger, Finite Element Methods for Viscous Incompressible Flows: a Guide to Theory, Practice, and Algorithms, Elsevier, 2012.
[14] Fukeng Huang, Jie Shen, Stability and error analysis of a class of high-order IMEX schemes for Navier-Stokes equations with periodic boundary conditions, SIAM J. Numer. Anal. 59 (2021) 2926–2954.
[15] Fukeng Huang, Jie Shen, Implicit-explicit BDFk SAV schemes for general dissipative systems and their error analysis, Comput. Methods Appl. Mech. Eng. 392 (0045–7825) (2022) 114718.
[16] S. Hugues, A. Randriamampianina, An improved projection scheme applied to pseudospectral methods for the incompressible Navier–Stokes equations, Int. J. Numer. Methods Fluids 28 (1998) 501–521.
[17] George Em. Karniadakis, Moshe Israeli, Steven A. Orszag, High-order splitting methods for the incompressible Navier-Stokes equations, J. Comput. Phys. 97 (2) (1991) 414–443.
[18] Michael Le Bars, David Cébron, Patrice Le Gal, Flows driven by libration, precession, and tides, Annu. Rev. Fluid Mech. 47 (1) (2015) 163–193.
[19] Xiaoli Li, Jie Shen, Error analysis of the SAV-MAC scheme for the Navier-Stokes equations, SIAM J. Numer. Anal. 58 (5) (2020) 2465–2491.
[20] Lianlei Lin, Zhiguo Yang, Suchuan Dong, Numerical approximation of incompressible Navier-Stokes equations based on an auxiliary energy variable, J. Comput. Phys. 388 (2019) 1–22.
[21] Yufeng Lin, Jérôme Noir, Libration-driven inertial waves and mean zonal flows in spherical shells, Geophys. Astrophys. Fluid Dyn. 115 (3) (2021) 258–279.
[22] Jian-Guo Liu, Jie Liu, Robert L. Pego, Stability and convergence of efficient Navier-Stokes solvers via a commutator estimate, Commun. Pure Appl. Math. 60 (10) (2007) 1443–1487.
[23] Roger Peyret, Spectral Methods for Incompressible Viscous Flow, vol. 148, Springer Science & Business Media, 2013.
[24] J. Shen, T. Tang, L.L. Wang, Spectral Method: Algorithms, Analysis and Applications, vol. 41, Springer, New York, 2011.
[25] J. Shen, J. Xu, J. Yang, The scalar auxiliary variable (SAV) approach for gradient flows, J. Comput. Phys. 353 (2018) 407–416.
[26] J. Shen, J. Xu, J. Yang, A new class of efficient and robust energy stable schemes for gradient flows, SIAM Rev. 61 (3) (2019) 474–506.
[27] Jie Shen, Efficient spectral-Galerkin method. I. Direct solvers of second- and fourth-order equations using Legendre polynomials, SIAM J. Sci. Comput. 15 (6) (1994) 1489–1505.
[28] R. Temam, Sur l'approximation de la solution des équations de Navier-Stokes par la méthode des pas fractionnaires. I, Arch. Ration. Mech. Anal. 32 (1969) 135–153.
[29] R. Temam, Navier-Stokes Equations: Theory and Numerical Analysis, North-Holland, Amsterdam, 1984.
[30] K. Wu, B.D. Welfert, J.M. Lopez, Librational forcing of a rapidly rotating fluid-filled cube, J. Fluid Mech. 842 (2018) 469–494.
[31] K. Wu, B.D. Welfert, J.M. Lopez, Precessing cube: resonant excitation of modes and triadic resonance, J. Fluid Mech. 887 (2020) A6.
[32] K. Wu, B.D. Welfert, J.M. Lopez, Reflections and focusing of inertial waves in a librating cube with the rotation axis oblique to its faces, J. Fluid Mech. 895 (2020) A5.
[33] Rakesh K. Yadav, Thomas Gastine, Ulrich R. Christensen, Scott J. Wolk, Katja Poppenhaeger, Approaching a realistic force balance in geodynamo simulations, Geophys. Astrophys. Fluid Dyn. 113 (43) (2016) 12065–12070.